Available online at www.sciencedirect.com
ScienceDirect
Journal of Power Sources 171 (2007) 634–643
JOURNAL OF POWER SOURCES
www.elsevier.com/locate/jpowsour

A dynamic 1D model of a solid oxide fuel cell for real time simulation

Denver F. Cheddie *, Norman D.H. Munroe

Applied Research Center, CEAS 2103, Florida International University, Miami, FL 33174, United States

Received 26 March 2007; received in revised form 19 June 2007; accepted 19 June 2007
Available online 28 June 2007

Abstract

A 1D dynamic solid oxide fuel cell (SOFC) model has been developed for real time applications. The model accounts for all transport and polarization phenomena by developing a system of governing differential equations over 1D control volumes. The 1D model is an improvement over existing 0D real time models in that it can more accurately predict the temperature and pressure variations along the cell while maintaining real time capabilities with regards to computational time. Several simplifications are required to maintain real time capabilities while improving the fidelity of the model.

It was found that a 1D model with 21 nodes performs each time dependent computation in 3.8 ms. Results show that activation overpotentials account for most of the total cell overpotential, and that temperature variations across this particular cell exceed 100 K. Depending on the gas channel configuration, the pumping power required to supply air and fuel to the cell can be in the same order of magnitude as the power produced by the fuel cell. It is shown that the use of fewer channels with larger cross-sectional areas, reduces the pressure drop due to wall friction, and hence reduces the required pumping power.

Keywords: Real time; SOFC model; 1D simulation

1. Introduction

Solid oxide fuel cells (SOFC) are considered prime candidates for stationary power generation in the intermediate to long-term future. In addition to its clean and efficient operation, its high temperature of operation (800–1100 K) allows for use of a wide range of fuels (including CO), as well as the possibility of heat recovery and co-generation. Because of its high tolerance to impurities in the fuel, e.g. CO and S, as compared to polymer electrolyte membrane (PEM) fuel cells—SOFCs can also be used in hybrid power generating systems. It can be coupled with a gas turbine or a biomass gasifier, and as such can be integrated with other renewable technologies.

Fuel cell modeling plays a critical role in the development of fuel cell technology. Fuel cell models can be broadly categorized as transport models or system models. Transport models provide a more detailed analysis of the transport phenomena occurring within the cell and can be used to optimize cell design and operating conditions. System models simulate the behavior of the fuel cell within the overall power generating system.

System models are not as comprehensive as transport models because they do not require the details of the cell's internal phenomena, only the input/output characteristics. Transport models can range from 1D to 3D and may by steady state or transient [1–8]. System models are usually 0D (lumped) or 1D to minimize the memory and computational time requirements, and are almost always transient [8–11]. In a system model, it is usually required that the computations be performed hundreds of times, therefore it is required to keep the memory requirements and computational times to a minimum. Further discussion of transport and system modeling is given in Bove and Ubertini [12] and Liese et al. [13].

Real time modeling is a special category of system modeling where the fuel cell model operates in real time, while fully interacting with other equipment within the system. This requires that the time dependent computations be performed within a specified period of time—typically in the order of milliseconds.

* Corresponding author. Tel.: +1 786 877 9235; fax: +1 305 348 6142.
E-mail addresses: dcheddie@yahoo.com (D.F. Cheddie), munroen@fiu.edu (N.D.H. Munroe).

0378-7753/$ – see front matter © 2007 Elsevier B.V. All rights reserved.
doi:10.1016/j.jpowsour.2007.06.170

Nomenclature

Arabic symbols

A	area (m^2)
c_p	specific heat capacity ($J\,kg^{-1}\,K^{-1}$)
D	diffusivity ($m^2\,s^{-1}$)
E	Activation Energy ($J\,mol^{-1}$)
f	friction factor
F	Faraday constant ($96485\,J\,mol^{-1}$)
h	heat transfer co-efficient ($W\,m^{-2}\,K^{-1}$)
I	cell current (A)
k	thermal conductivity ($W\,m^{-1}\,K^{-1}$)
K	exchange current density term ($S\,m^{-2}$)
L	length (m)
m	mass flow rate ($kg\,s^{-1}$)
N	number
P	pressure (Pa)
Q	heat generation (W)
R	universal gas constant ($8.3143\,J\,mol^{-1}\,K^{-1}$)
Re	Reynolds number
t	time (s)
T	temperature (K)
u	velocity ($m\,s^{-1}$)
V	potential (V)
w	width (m)
x	mole fraction, displacement in the direction of the gas channel (m)

Greek symbols

λ	stoichiometric rate
μ	dynamic viscosity (Pa s)
ρ	density ($kg\,m^{-3}$)
τ	thickness (m)
ω	mass fraction

Subscripts and superscripts

act	activation
an	anode
atm	atmospheric
ca	cathode
ch	channel
el	electrode
gen	generated
i	species
int	interconnect
ohm	ohmic
pen	positive-electrolyte-negative
0	reference state

Most system models are designed to perform computations in the order of seconds and minutes. In fact most system models are designed to minimize memory requirements rather than maximize speed. The precise time frame which defines "real time" depends on the other equipment in a fuel cell system. In this work, it depends on the compressor valve timing, which is approximately 5 ms.

The hardware-in-the-loop (HIL) concept makes use of real and virtual components of the fuel cell system. In the example of a turbine/SOFC hybrid, the turbine power plant comprises the real components. The real time fuel cell model comprises the virtual components. Thus the model operates in lieu of a real fuel cell stack, and interacts in real time with the other components. The other components operate as if there were, in fact, an actual fuel cell stack present. Thus, for HIL purposes, it is critical that the model operates in real time. The fact the real time model must fully interact with other equipment means that cell voltage and current are not the only input/output parameters of interest. Also important are input and output temperatures, pressures, concentrations and flow rates. The output from the model is inputted into real components, which then perform as though there were in fact a fuel cell present outputting at a given temperature, pressure, concentration and flow rate. So in addition to current/voltage, the real time model is also interested in various transport properties.

It is believed that hybrid fuel cell systems will play a prominent role in the intermediate future as fuel cell technology slowly makes its way into the market, and real time modeling will become increasingly important. Most of the system models developed are designed to deliver "fast" computations, but not fast enough for real time simulation. Most system models perform the necessary computations in the order of seconds. Real time models, therefore, must be simplified to allow for computational times in the order of milliseconds. For this reason, most real time models are 0D [14,15]. The most popular hybrid system investigated is the SOFC/gas turbine system [16,17], however biomass/SOFC systems have also received some attention [18]. In the literature, real time models for hybrid power generating systems have focused on control systems [19] and have covered a wide range of applications including aerospace applications [20].

This work presents a 1D real time model, which is designed to improve the fidelity of real time modeling, while maintaining the necessary computational times. As mentioned earlier, the fidelity of the model must be measured in terms of its ability to predict the electrochemical as well as the transport performance of the fuel cell. Results are validated by comparing the prediction of the real time model to those of a fully resolved model using a finite element mesh with iterative solvers. The model used to perform the validation is much more comprehensive and does not make many of the limiting assumptions of the real time model discussed in this paper. Thus, we are validating how well the real time model compares with a more comprehensive model of the same problem. The model is presented here for a planar cell, however, it can be applied to any type of SOFC design.

2. Model development

2.1. Assumptions and simplifications

Compared to other system models, real time models must be simplified in order to perform the computations within the necessary time frame. However, compared to existing 0D real time models, the present 1D model is an improvement with regard

to accuracy, while maintaining real time capability. This section discusses some of the simplifications employed in the present model.

The gas channel and interconnect are integrated at both the fuel and oxidant side. The treatment is still 1D, but the channel and interconnect states are not separated. For example, the results presented by Aguiar et al. [7] show a difference between the interconnect temperature and the fluid temperature in the channels. This work treats the channel/interconnect as one integrated domain.

The anode, cathode and electrolyte are similarly integrated into one region. This region is called the PEN. For the purpose of calculating pressure drops in the porous electrode regions, the thicknesses of the anode and cathode are used. However, there is no distinction made between the electrolyte temperature and the electrode temperature.

To reduce the number of computations, a uniform distribution of current density is assumed. The average current density is assumed to exist at all points. This way there is no need to iteratively calculate the cell current or voltage. This is in contrast to numerous models which assume equipotential conditions with a spatial variation in current density. These models, hence will be more accurate, but it will be seen in Section 3 that the inaccuracy of the present model is not severely compromised by this assumption. On the other hand its computational speed is greatly enhanced. Multi-dimensional models, and even the 1D model by Aguiar et al. [7] require an iterative solver to converge upon the correct solution to the electrochemical problem. This is not amenable to real time simulation, since the iterative procedure is the primary time consumer in the solution process.

For the purpose of the present model, it is not necessary to know the overpotentials at each node, only the average overpotentials across the cell. The reversible potential as well as the activation and ohmic overpotentials depend on temperature and partial pressure. The temperature and pressure will be computed at each node, however, to determine the necessary potentials and overpotentials, the average PEN temperature and partial pressures will be used.

Following the previous two simplifications, the heat generation due to cell irreversibilities is also assumed to be uniformly distributed and equal at each nodal point. Also uniform heat and mass transfers between the PEN and the channel is assumed at each node.

Due to the relative time scales, the electrochemical problem is assumed to occur instantaneously (or in steady state). It is assumed that the voltage immediately responds to changes in current. However, the thermal problem takes a longer period of time to reach steady state conditions, and the electrochemical problem depends on temperature. So the potentials are considered to depend on time only as the temperature depends on time.

2.2. Electrochemical model

The following half-cell reactions take place at the anode and cathode, respectively:

$$2H^2 + 2O^{2-} \rightarrow 4e^- + 2H_2O \quad (1)$$

$$O_2 + 4e^- \rightarrow 2O^{2-} \quad (2)$$

In this model, the cell current is specified and the cell overpotentials are then determined. The reversible cell potential can be determined from Eqs. (3) and (4) [14]:

$$E = E_0 + \frac{RT}{2F}\ln\left(\frac{P_{H_2}P_{O_2}^{0.5}}{P_{H_2O}P_{atm}^{0.5}}\right) \quad (3)$$

$$E_0 = 1.2877 - (2.904 \times 10^{-4})T \quad (4)$$

The average channel partial pressures are used in Eq. (3). The PEN temperature is used since that is where the electrochemical reactions occur. To determine the concentration overpotential, the average partial pressures in the PEN can be substituted in Eq. (3). The concentration overpotential is taken as the difference in values obtained by using the channel pressures and the PEN pressures in Eq. (3).

The average PEN partial pressure of species, i, can be determined from its average partial pressure in the channel using Fick's law of diffusion, assuming that convection is negligible within the porous electrodes. Previous works consider the gas concentration as a function of partial pressure only [7,8]. However, based on the ideal law, gas concentration is a function of partial pressure and temperature:

$$\frac{P_i^{pen}}{RT_{pen}} = \frac{P_i^{ch}}{RT_{ch}} + \frac{\overset{o}{m}_i}{M_i}\frac{\tau}{D_i} \quad (5)$$

The ohmic overpotential is a function of current density and temperature. Eq. (6) includes the PEN resistance as well as the interconnect resistance [7,21]:

$$\eta_{ohm} = i\left[(6.78 \times 10^{-10})\exp\left(\frac{10.3 \times 10^3}{T}\right) + (0.23174)\exp(-0.0115T)\right] \quad (6)$$

The expressions for the activation overpotentials are taken from Liese et al. [14]. It is assumed that there is no partial pressure dependence at the cathode. The exchange current density is given by Eq. (9). In Eqs. (7) and (8), the PEN partial pressures are used. The PEN subscript is not shown to avoid over complicating the equations:

$$\eta_{act}^{an} = \frac{RT}{F}\left[\sinh^{-1}\left(\frac{i/2i_0}{\{(P_{H_2}/P_{H_2}^{ref})(P_{H_2O}/P_{H_2O}^{ref})\}}\right) - \frac{1}{2}\ln\left(\frac{P_{H_2}/P_{H_2}^{ref}}{P_{H_2O}/P_{H_2O}^{ref}}\right)\right] \quad (7)$$

$$\eta_{act}^{ca} = \frac{RT}{F}\left[\sinh^{-1}\left(\frac{i}{2i_0}\right)\right] \quad (8)$$

$$i_0 = \frac{RT}{nF}K_{el}\exp\left(-\frac{E_{el}}{RT}\right) \quad (9)$$

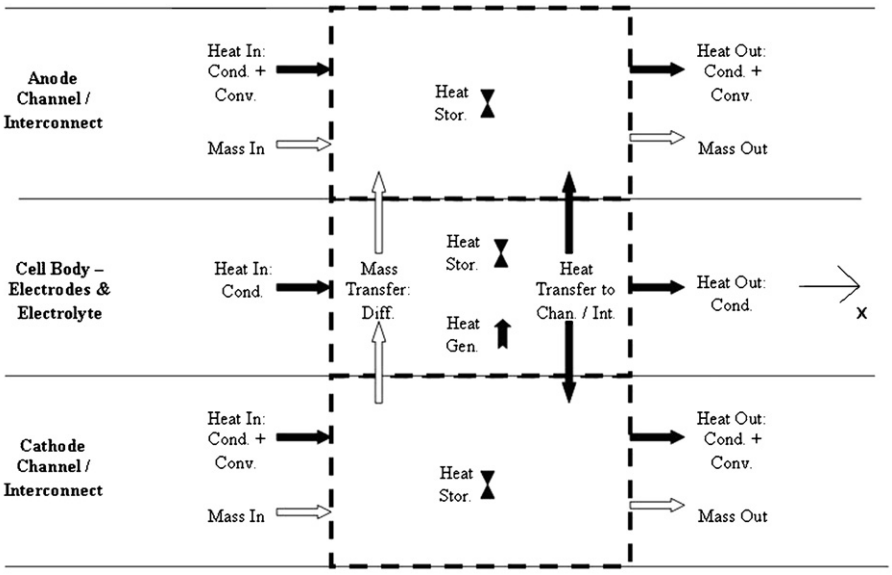

Fig. 1. Energy and mass balances over 1D control volumes.

2.3. Transport model

The transport equations are developed based on mass and energy balances over the 1D nodal control volumes shown in Fig. 1. Because there is mass transfer between the channels and the PEN, there is a non-zero source term in the continuity equation (10). This source term is needed to account for mass transfer in the orthogonal directions:

$$\frac{\partial(\rho u)}{\partial x} = -\frac{\partial \rho}{\partial t} + \frac{\sum \overset{\circ}{m}_i}{A_{\mathrm{ch}} L_{\mathrm{cell}}} \tag{10}$$

The sign convention used in this work is such that a vector quantity is considered positive when the direction is into the domain, and negative out of the domain. The rates of diffusion of each individual species in the PEN are as follows:

$$\overset{\circ}{m}_{\mathrm{H_2O}} = \frac{I M_{\mathrm{H_2O}}}{2F} \tag{11}$$

$$\overset{\circ}{m}_{\mathrm{H_2}} = -\frac{I M_{\mathrm{H_2}}}{2F} \tag{12}$$

$$\overset{\circ}{m}_{\mathrm{O_2}} = -\frac{I M_{\mathrm{O_2}}}{4F} \tag{13}$$

The diffusion of hydrogen and oxygen are considered negative because they flow out of the channel domains, while water vapor flows into the anode channel domain:

$$\frac{\partial P}{\partial x} = -\frac{\partial(\rho u)}{\partial t} + \frac{\partial(\rho u)^2}{\partial x} + \frac{\sum \overset{\circ}{m}_i u}{A_{\mathrm{ch}} L_{\mathrm{cell}}} - \left[\left(\frac{\tau_{\mathrm{ch}}}{w_{\mathrm{ch}}}\right)^{1/2} + \left(\frac{w_{\mathrm{ch}}}{\tau_{\mathrm{ch}}}\right)^{1/2}\right] f\,Re_{\sqrt{\tau_{\mathrm{ch}} w_{\mathrm{ch}}}} \frac{\mu N_{\mathrm{ch}}}{A_{\mathrm{ch}}} u \tag{14}$$

The momentum equation (14) is based on the Navier–Stokes equations applied over 1D. Wall friction is based on the velocity gradients in the directions perpendicular to the solid surfaces, thus the viscous terms must be modified to properly account for wall friction in the channels. It can be shown that for a rectangular channel, the last term in Eq. (14) accounts for the pressure drop due to Darcy friction, assuming laminar flow. Eq. (15) gives the dimensionless product of the friction factor and Reynold's number based on analytical correlations given in [22]. The Reynold's number is based on the square root of the channel cross sectional area. Note that the A_{ch} in Eq. (14) refers to the total cross-sectional area of all of the channels, so that equation is modified by multiplying by the total number of channels.

The energy Eqs. (16) and (17) govern the thermal problem. All of the heat generation is assumed to occur in the PEN, where conduction is dominant and convection is considered negligible. The channel/interconnect cross-sectional area ratio occurring in the first term on the RHS of Eq. (16) arises due to the integration of the channel and interconnect domains. It can also be seen from these equations that heat conduction is considered negligible in the fluid phase, due to the fact that the thermal conductivity is much higher in the solid regions than in the fluid phases. The same is true of the heat storage due to higher volumetric heat capacities (ρc_p) of the solid regions. Also the sign convention of positive heat and mass transport into the domains are maintained:

$$(\rho c_p)_{\mathrm{int}} \frac{\partial T_{\mathrm{int}}}{\partial t} = -\frac{\partial(\rho u c T_{\mathrm{int}})}{\partial x} \frac{A_{\mathrm{ch}}}{A_{\mathrm{int}}} + k_{\mathrm{int}} \frac{\partial^2 T_{\mathrm{int}}}{\partial x^2} + \frac{\sum \overset{\circ}{m}_i c_i T_{\mathrm{int}} + h A_{\mathrm{cell}} (T_{\mathrm{pen}} - T_{\mathrm{int}})}{A_{\mathrm{int}} L_{\mathrm{cell}}} \tag{16}$$

$$f\,Re_{\sqrt{t_{\mathrm{ch}} w_{\mathrm{ch}}}} = \frac{12}{\left[1 - (192/\pi^5)(\tau_{\mathrm{ch}}/w_{\mathrm{ch}}) \tanh((\pi/2)(w_{\mathrm{ch}}/\tau_{\mathrm{ch}}))\right](1 + (\tau_{\mathrm{ch}}/w_{\mathrm{ch}}))\sqrt{\tau_{\mathrm{ch}}/w_{\mathrm{ch}}}} \tag{15}$$

$$(\rho c_p)_{\text{pen}} \frac{\partial T_{\text{pen}}}{\partial t} = k_{\text{pen}} \frac{\partial^2 T_{\text{pen}}}{\partial x^2} + \frac{Q_{\text{gen}} - \sum \dot{m}_i c_i T_{\text{int}} - hA_{\text{cell}}(T_{\text{pen}} - T_{\text{int}})}{A_{\text{pen}} L_{\text{cell}}} \quad (17)$$

The heat generation in the cell can be determined from first and second law thermodynamic analyses of the fuel cell. The heat is due to irreversibilities due to the total cell overpotential and entropy changes. The entropy change for the fuel cell reaction can be correlated from thermodynamic tables and expressed as a function of temperature. This expression is given in Eq. (19):

$$Q_{\text{gen}} = I\left(V_{\text{rev}} - V_{\text{cell}} - \frac{T\,\Delta S}{nF}\right) \quad (18)$$

$$\frac{\Delta S}{n} = -(23.328 + 0.0042T)\,(\text{J mol}^{-1}\,\text{K}^{-1}) \quad (19)$$

The Stefan–Maxwell equation (20) is used to describe the transport of individual species in the gas channels. The species considered are H_2, CO_2 and H_2O at the anode; and O_2 and N_2 at the cathode. In this paper, it is assumed that the fuel is externally reformed resulting in an inlet fuel stream consisting of H_2, CO_2 (inert) and H_2O. No direct internal reforming is considered in this paper, as that will be addressed in a later work.

The last term in Eq. (20) is the source/sink term which represents mass diffusion between the channels and the PEN. No electrochemical reactions take place in the channels, but it is assumed that all of the net mass of a species diffusing from the channel to the PEN eventually reacts:

$$\rho \frac{\partial w_i}{\partial t} = -\frac{\partial(\rho u w_i)}{\partial x} + D_i \frac{\partial^2(\rho w_i)}{\partial x^2} + \frac{\dot{m}_i}{A_{\text{ch}} L_{\text{cell}}} \quad (20)$$

Finally the gas mixture density is given by the ideal gas relation:

$$\rho = \frac{PM}{RT} = \frac{P}{RT}\left(\sum \frac{\omega_i}{M_i}\right)^{-1} \quad (21)$$

2.4. Boundary conditions

The boundary conditions at node 1 are specified from the inlet gas conditions. The anode and cathode gas temperatures, mass fractions, pressures and flow rates are given (Dirichlet). The PEN temperature at node 1 is not specified, but assuming negligible heat losses at the ends of the cell, insulation conditions exist (Neumann).

The same is true of the PEN at the final node. For the channel/interconnect, it is assumed that heat and mass exit the cell solely via convection, i.e. heat conduction and mass diffusion are zero at the outlet (Neumann conditions).

Tables 1–3 list the numerical values used for base calculations in the present model. These numerical values are for the most part the same as those used by Aguiar et al. [7].

Table 1
Cell geometries [7]

Number of channels per cell	50
Cell length	0.4 m
Cell width	0.1 m
Channel thickness	0.5 mm
Channel width	1 mm
Interconnect thickness	2.5 mm
Anode thickness	500 μm
Cathode thickness	50 μm
Electrolyte thickness	20 μm

Table 2
Cell constants [7]

	Anode	Cathode
T_{in} (K)	1023	1023
P_{in} (atm)	1	1
K_{el} (S m^{-2})	6.54×10^{11}	2.35×10^{11}
E_{el} (kJ mol^{-1})	140	137
λ	1.33	8.93
h (W m^{-2} K^{-1})	302	302
D (m^2 s^{-1})	3.66×10^{-5}	1.37×10^{-5}

	Interconnect	PEN
ρc_p (MJ m^{-3} K^{-1})	4	2.95
k (W m^{-1} K^{-1})	25	2

2.5. Solution methodology

It is noticed from Eqs. (10) and (14) that the transient term in the continuity and momentum equations are placed on the RHS rather than the LHS. This was done deliberately to allow for greater stability in the solution process. The momentum equation (14), for example, has two dominant terms—the pressure gradient and the Darcy friction. Placing the transient term on the LHS requires very precise initial guesses, which place severe limitations on the model. There would also be numerical stability problems when rapid changes in loading conditions are applied. Physically, it is best to understand the momentum equation as a formula for calculating the pressure drop given the velocity profile.

Recall that in the present model, iterative solution procedures are avoided. Iterative procedures require time to converge, and are thus not amenable to real time modeling. An explicit solution scheme is preferred, which allows the model to calculate the next time parameters given the present state variables and derivatives. It is assumed that the necessary history of the cell

Table 3
Gas properties [23]

	Inlet mole fraction, x	Specific heat capacity, c_p (J kg^{-1} K^{-1})	Dynamic viscosity, μ (Pa s)
H_2	0.571	$13960 + 0.950T$	$5.24 + 0.0156T$
H_2O	0.286	$1639.2 + 0.641T$	$-9.56 + 0.3603T$
CO_2	0.143	$804 + 0.460T$	$70.40 + 0.3340T$
O_2	0.21	$876.80.217T$	$146.38 + 0.3330T$
N_2	0.79	$935.6 + 0.232T$	$129.22 + 0.2725T$

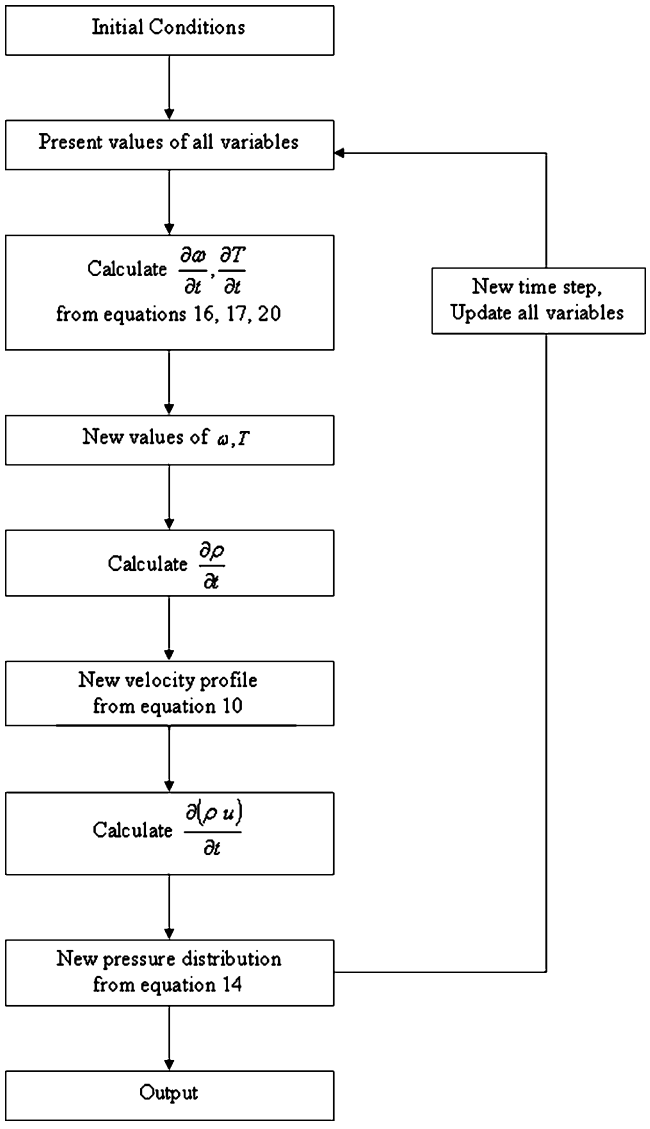

Fig. 2. Solution algorithm.

can be captured by its present state variables and time derivatives. The solution algorithm is shown in Fig. 2. The model is solved in Matlab/Simulink using the 4th order Runge–Kutta method to solve the time dependent problem. The fully resolved model used to validation of the real time model is generated for a finite element mesh, and solved iteratively using FEMLAB® 3.1. All computations are conducted on a 1GB, 3GHz Pentium 4 processor.

3. Results

3.1. Computational time

Fig. 3 shows the variation of the steady state channel outlet temperatures as the number of nodal points in the model varies. As expected, as the number of nodes increases, the solution converges to the point of grid independence. It shows that using less than 10 nodes results in large inaccuracies. In this range, the solution is very grid dependent. However, as the number of nodes increases above 20, the solution becomes less grid dependent. In fact, there is very little difference in accuracy between a model with 21 nodes and one with 51 nodes. A model with 2 or 3 nodes approaches a 0D model. These results clearly illustrate that a 1D model greatly improves the accuracy compared with a 0D model.

Fig. 3 also shows the computational times required to perform each time dependent iteration. This value increases approximately to the 1.5 power of the number of nodes. Given that 5 ms is the desired maximum computational time per iteration, the model with 21 nodes provides the optimum balance between speed (3.8 ms) and accuracy. Its accuracy is not very different from one with 51 nodes, but its computational time is significantly lower. Thus a 1D model with 21 nodes improves the accuracy of 0D models while maintaining real time capabilities, and thus 21 is chosen as the optimum number of nodes and will be used for the remainder of results presented. Note that the number of nodes is chosen as 21 so that there will be 20 spatial divisions.

3.2. Model validation

Validation of the time dependent model is done by comparing numerical results with the results of a fully resolved model for the same set of operating conditions and cell geometries. This fully resolved model uses an iterative technique to solve for the current density distribution for a specified set of equipotential condition. This is done to ensure that the limiting assumptions made in the real time model did not significantly affect the results. Figs. 4 and 5 show that the inaccuracies introduced by this assumption only resulted in an error in the order of 1%. However, the more comprehensive model requires computational times between 2 and 3 s for a 1D domain. This far exceeds the requirements for real time modeling. These figures show that the real time model's accuracy is not significantly compromised by the simplifying assumptions.

Fig. 4 shows the dynamic voltage response to changes in cell current. Initially, steady state conditions were allowed for a cell current density of 0.5 A cm^{-2} (cell current of 200 A). Then the current density is suddenly changed to each of the other values shown in the figure. Consistent with model assumptions, when

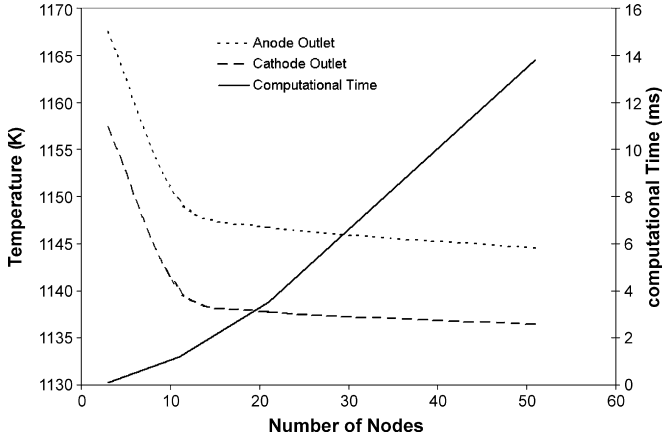

Fig. 3. Solution accuracy and computational times vs. the number of nodes.

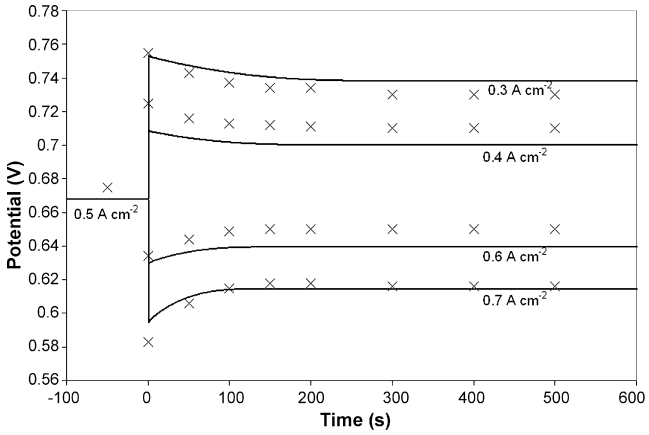

Fig. 4. Dynamic cell potential response to change in loading conditions (constant heat capacity).

the current density changes, the voltage immediately responds. However, because the temperature takes a longer period of time to reach steady state, the voltage slowly stabilizes as the temperature varies with time. Thus, there is the expected overshoot and undershoot of the cell voltage followed by a period of stabilization.

3.3. Thermal analyses

The results in Fig. 4 are based on the assumption that the specific heat capacity of the gases do not change significantly over the length of the cell—an assumption made by Aguiar et al. [7]. So Fig. 4 was produced using the heat capacity values based on the inlet temperatures just to compare with their model. In reality, heat capacity is a function of temperature, and the temperature variation across the length of the cell can be in the order of 100 K. Table 3 shows the heat capacity correlations used in this work. For the case where "constant heat capacity" is used, the specific heat capacity was mass averaged at both the anode and cathode inlets. In the case where "variable heat capacity" was used, the heat capacity is mass averaged at every node, taking into account composition and temperature effects. Fig. 5 shows the transient voltage response to the same changes

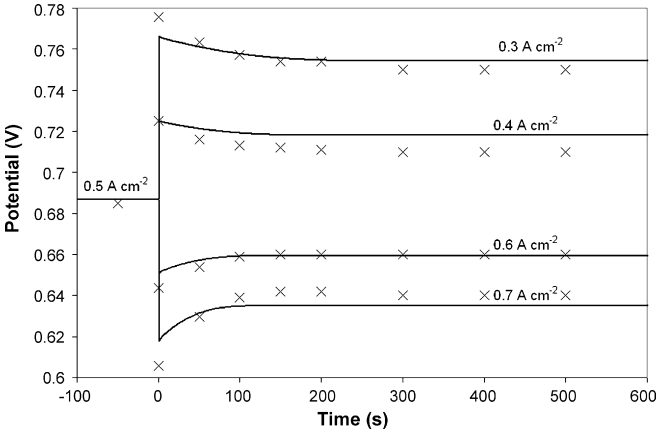

Fig. 5. Dynamic cell potential response to load changes (heat capacity as a function of temperature and composition).

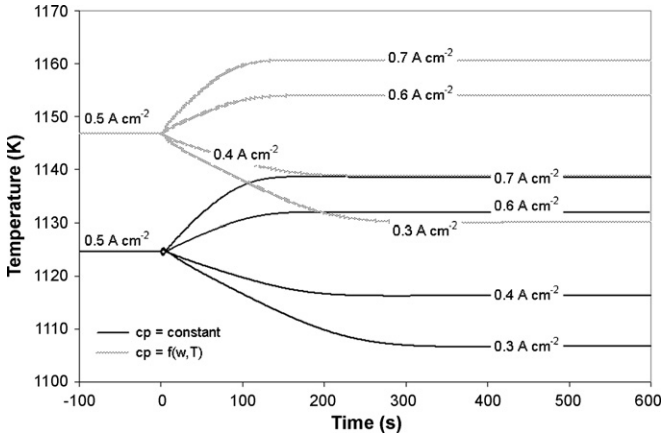

Fig. 6. Dynamic anode outlet temperature response to load changes.

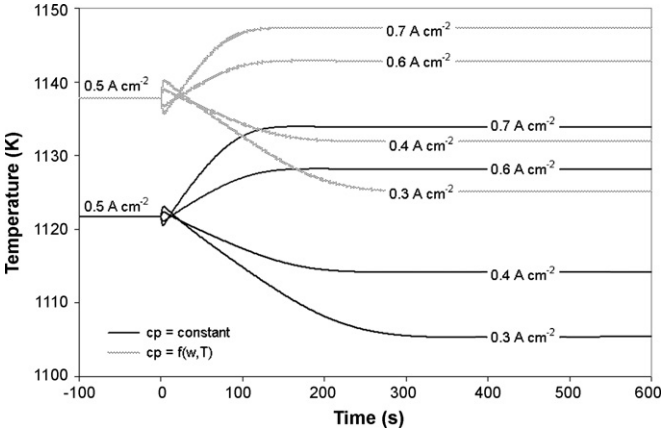

Fig. 7. Dynamic cathode outlet temperature response to load changes.

in current density as in Fig. 4, this time with gas species heat capacity as functions of temperature. The overall mixture heat capacity is a function of temperature and gas composition. It can be seen that the voltages are slightly higher than those in Fig. 4. The reason for this is that the temperature distribution is altered by the assumption of variable heat capacity, hence the potentials and overpotentials are also altered.

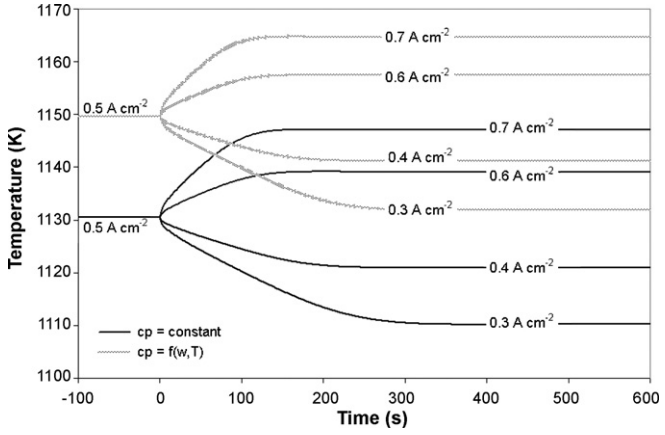

Fig. 8. Dynamic PEN (maximum) temperature response to load changes.

Figs. 6–8 show the dynamic temperature response to the identical changes in current density, for both cases of constant and variable heat capacity. They all show that the outlet temperatures of the channels as well as the maximum PEN temperature increase when variable heat capacities are taken into account. From the heat capacity correlations in Table 3, all of the gas heat capacities increase with temperature. One would expect that if the heat capacity increases, then the outlet temperatures should decrease. The reason the temperatures actually increase is because the mixture heat capacity of the anode decreases considerably along the channel. Since hydrogen is being consumed, and the hydrogen heat capacity is much higher than the other gases, the decreasing hydrogen mass fraction results in a decreasing mixture heat capacity along the anode channel. Fig. 9 shows the spatial variation in mixture heat capacity along the gas channels. The cathode channel heat capacity only slightly increases along the channel, whereas the anode heat capacity decreases significantly as the hydrogen composition diminishes. Since the temperatures at both channels and the PEN are all interrelated, the net effect is that all of the temperature variables increase when the heat capacity is considered a function of temperature. One would expect that this consideration would improve the accuracy of the model.

It is noticeable, comparing Figs. 6 and 7, that the anode channel outlet has a higher temperature than the cathode. It is true, for a SOFC that the reaction heat is more concentrated on the anode side, however the present model, which integrates the entire PEN region, does not "know" this. The reason the anode has a higher temperature than the cathode is because of the lower flow rates used there. Table 4 shows that the volumetric flow rates at the cathode are an order of magnitude higher than those at the anode. This is because the stoichiometric rates are higher at the cathode. The anode stoichiometry is chosen for optimum fuel utilization, while the cathode stoichiometry is chosen to reduce the temperature.

Another noticeable feature of Fig. 7 is the kink in the temperature variation at the instant the current density changes. This kink exists because the cell current is assumed to change instantaneously, and as a result the rate of mass diffusion between the channels and the PEN also changes instantly. When the current suddenly increases, the rate at which the cathode channel loses energy instantly increases, which results in an initial tendency for the temperature to drop. However, because more heat is produced in the cell when the current increases, the long-term trend is for the temperature to increase. The kink represents a conflict between the initial loss of energy and the long-term increase in heat generation.

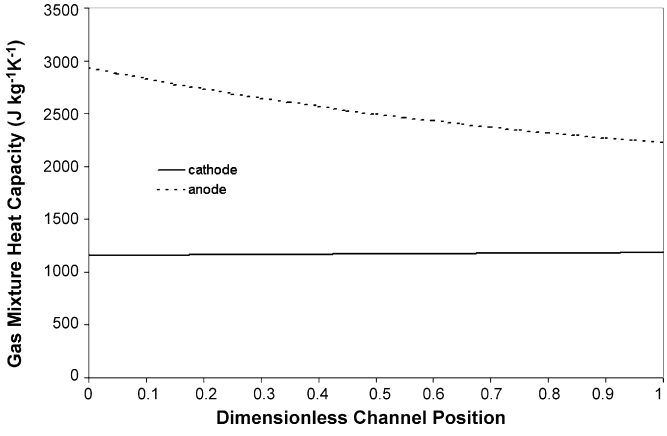

Fig. 9. Variation of steady state mixture heat capacity along the gas channels.

Table 4
Parametric model outputs for various input conditions

Inlet temperature (K)	1023 (base)	973	1073	1023
Inlet pressure (mV)	1	1	1	3.6
Cell power (mV)	137.4	120.4	149.2	153.6
Cell potential (mV)	687.0	602.0	746.0	767.9
Reversible potential (mV)	918.4	931.8	903.9	950.2
Activation overpotential (mV)	180.8	260.7	119.9	129.5
Ohmic overpotential (mV)	43.1	62.2	29.8	45.4
Concentration overpotential (mV)	7.5	6.9	8.2	7.5
Anode outlet temperature (K)	1144.9	1114.5	1181.0	1134.3
Cathode outlet temperature (K)	1137.3	1105.9	1174.0	1127.3
Maximum PEN temperature (K)	1147.9	1117.5	1183.9	1137.1
Heat generation (W)	109.2	126.2	97.4	99.0
Anode heat gain (W)	28.3	29.5	27.9	26.9
Cathode heat gain (W)	81.6	97.5	70.1	72.7
Anode pressure drop (kPa)	8.6	7.9	9.3	2.4
Cathode pressure drop (kPa)	92.1	85.7	98.9	25.5
Anode inlet volumetric flow rate ($cm^3\ s^{-1}$)	203.1	193.1	213.0	56.4
Cathode inlet volumetric flow rate ($cm^3\ s^{-1}$)	1850.3	1759.8	1940.7	514.0
Required pumping power (W)	172.1	152.3	194.0	13.2

3.4. Parametric analyses

Table 4 shows the breakdown of steady state cell parameters for various inlet conditions. The second column (inlet temperature of 1023 K) represents the base case condition. For a current density of 0.5 A cm^{-2}, the cell potential is 0.687 V resulting in 137.4 W of electrical power and 109.2 W of heat generation. The overpotentials are dominated by the activation overpotential, which constitutes 0.181 V.

As the inlet temperatures increase, the reversible potential decreases, as one would expect from Eq. (4). However, the cell potential increases because the activation and ohmic overpotentials decrease with temperature. The concentration overpotential increases slightly with temperature because, according to Eq. (5), the reactant concentrations decrease slightly as the temperature increases. When the inlet pressure increases, the reversible potential predictably increases, while the activation overpotential decreases, resulting in a net increase in cell voltage.

The computations for the base conditions show that the heat gains by the anode and cathode are 28.3 and 81.6 W, respectively, representing a 0.6% error in heat balance. The anode absorbs less heat than the cathode, yet attains a higher outlet temperature. The reason for this, as previously explained, is

Table 5
Effect of channel configuration

Number of channels	Channel thickness (mm)	Channel width (mm)	fRe [16]	Required pumping power (W)
50	0.5	1	16.457	172.1
50	0.75	1	14.568	64.5
50	1	1	14.132	34.8
25	1	2	16.457	21.5
10	1	5	25.569	17.0
5	1	10	36.807	15.8

the low flow rates existing at the anode. When the inlet temperatures are increased, there is an increase in heat generation primarily because of the high irreversibilities due to entropy changes. When the inlet pressure increases from 1 to 3.6 atm, there is a decrease in heat generation and outlet temperatures. This is because the better cell performance results in a higher cell potential and lower overpotentials. The lower total overpotential results in the lower heat generation value, and consequently, lower outlet temperatures.

3.5. Pumping power

The pressure drop along the channels and the required pumping power to overcome this pressure drop have not been given much attention in previous works. However given the numbers in Table 4, this represents a major loss. For the channel geometries given, the computed pressure drop across the cathode is a staggering 92.1 kPa for the base condition. The 8.6 kPa drop across the anode is because of the lower flow rate. For the necessary volumetric flow rates, the total pumping power required to supply the anode and cathode gases to the cell is 172.1 W per cell. Considering that the cell power output is 137.4 W, the given cell uses more energy than it produces. The other results show that the pressure drop increases with temperature, perhaps because higher temperatures result in lower gas densities, which result in higher velocities, and hence larger wall friction losses. When the inlet pressure in raised to 3.6 atm, the pressure drops and pumping power decrease significantly. The reasoning is similar. A higher pressure results in a higher gas density, which eventually reduces the effect of wall friction. Appendix A shows some rough "hand" calculations to verify the model results, and to show that for the given geometries and operating conditions, the pressure drops shown in Table 4 are indeed expected.

Clearly such a high amount of required pumping power is unacceptable. Table 5 shows the effect of configuring the channel geometry on the required pumping power. For each case, the cell power is the same as the base condition, 137.4 W. The top row represents the base condition, where there are 50 channels of 2×1 rectangular sections. For the base condition, as mentioned previously, the required pumping power is 172.1 W. Keeping the channel width fixed and increasing its thickness results in a decrease in pumping requirements. It is primarily because the larger channel area allows for lower velocities, hence lower pressure drops. Now keeping the channel thickness fixed at 1 mm and increasing the channel width (hence decreasing the number of channels), results in a further decrease in pumping requirements. Although the total cross-sectional area remains the same, fewer channels means fewer walls, hence lower pressure losses. These results indicate that as far as pumping requirements are concerned, having fewer thicker channels is the most optimal configuration.

The results presented in Table 5 do not take into account changes in the convective heat transfer coefficient incurred by the changes in geometry. It is known that the Nusselt number may vary by up to 100% over the geometries mentioned in Table 5. However, this does not significantly affect the temperature distribution. The heat generation is unaffected by changes in geometry, thus the only effect will be to minimize the difference between the interconnect/channel temperature and the PEN temperature. For the geometry shown in the bottom row of Table 5 (1×10 channel), the steady state temperatures predicted by the present model are: anode outlet (1145.8 K), cathode outlet (1137.7 K), PEN node 21 (1148.6 K). With a slight modification in the script, the effect of channel geometry on convective heat transfer coefficient can be taken into account. The respective steady state results are: anode outlet (1143.6 K), cathode outlet (1139.4 K), PEN node 21 (1144.9 K). It is clear that the effect of this phenomenon the temperature distribution is not significant. The difference between the three temperatures decreased, but not significantly.

4. Conclusion

A 1D SOFC model was developed for application in real time system simulation. The 1D model is an improvement over existing 0D real time models. Results showed that a model with 21 nodes offered the best balance between computational time and accuracy. Such a model required 3.8 ms of computational time for each time iteration, and offered grid independent solutions.

The model applied the principles of mass and energy conservation over 1D control volumes to arrive at a system of governing differential equations which were solved in Matlab/Simulink. Thus, the model was able to more accurately predict the transport phenomena than existing real time models. The model results showed that the expected temperature variations for the fuel cell in question are in the order of 100 K. Depending on the channel geometry, the required pumping power to overcome Darcy wall friction was in the same order of magnitude as the power produced by the cell. The model predicted that using fewer channels with larger cross sectional areas would significantly reduce the pressure drop and hence increase the net power produced by the cell.

Acknowledgement

The authors would like to express their gratitude for the support from the NSF CREST Supplement Grant (Award No. HRD-0317692) in conducting this work.

Appendix A

Rough calculations for the pressure drop and pumping requirements:

Channel thickness : $\tau_{ch} = 0.5e-3\,\text{m}$

Channel width : $w_{ch} = 1e-3\,\text{m}$

$f\,Re = 16.457$

Characteristic length for Reynold's number :

$$d = \sqrt{\tau_{ch} w_{ch}} = 0.71e-3\,\text{m}$$

At the cathode, for a cell current of 200 A, an inlet O_2 mass fraction of 0.22, and a stoichiometric rate of 8.93, the inlet flow rate at the cathode is

$$\rho u A_{ch} = 8.93 \times \frac{(200)\times(32e-3)}{4\times(96,485)}\frac{1}{0.22} = 6.73e-4\,\text{kg s}^{-1},$$

$$\rho = \frac{(1.013e5)\times(29.16e-3)}{(8.3143)\times(1023)} = 0.347\,\text{kg m}^{-3},$$

$$u = \frac{6.73e-4}{(0.347)\times(0.5e-6)\times(50)} = 77.5\,\text{m s}^{-1},$$

$$\mu \approx 4e-5\,\text{Pa s},$$

$$Re \approx \frac{(0.347)\times(77.5)\times(0.71e-3)}{4e-5} = 476$$

which verifies that the flow is laminar:

$$f \approx \frac{16.457}{476} = 0.035$$

The wall friction shear stress :

$$\sigma_{wall} \approx 0.035\frac{(0.347)\times(77.5)^2}{2} = 36.0\,\text{Pa}$$

Friction force per channel length

$$= (36.0)\times(1e-3+0.5e-3)\times 2 = 0.108\,\text{N m}^{-1}$$

Pressure drop per channel length

$$= \frac{0.108}{(1e-3)\times(0.5e-3)} = 216,058\,\text{Pa m}^{-1}$$

Over a length of 0.4 m, the pressure drop = 86,423 Pa = 86.42 kPa.

This is in the same order of magnitude as that predicted in Table 4.

The volumetric flow rate

$$= (77.5)\times(0.5e-6)\times(50) = 1.94e-3\,\text{m}^3\,\text{s}^{-1}$$

Thus the required pumping power for the cathode

$$= (1.94e-3)\times(86423) = 167.8\,\text{W}$$

These calculations show that the pressure drops and pumping requirements predicted by the model are accurate for the given cell geometries and operating conditions.

References

[1] E. Achenbach, J. Power Sources 491 (1994) 333–348.
[2] N.F. Bessette, W.J. Wepfer, J. Winnick, J. Electrochem. Soc. 142 (1995) 3792–3800.
[3] R. Suwanwarangkul, E. Croiset, M.W. Fowler, P.L. Douglas, E. Entchev, M.A. Douglas, J. Power Sources 122 (2003) 9–18.
[4] J.R. Ferguson, SOFC two dimensional "unit cell" modeling. SOFC Stack Design Tool, International Energy Agency Final Report, 1992.
[5] L. Petruzzi, S. Cocchi, F. Fineschi, J. Power Sources 118 (2003) 96–107.
[6] S.B. Beale, Y. Lin, S.V. Zhubrin, W. Dong, J. Power Sources 118 (2003) 79–85.
[7] P. Aguiar, C.S. Adjiman, N.P. Brandon, J. Power Sources 147 (2005) 136–147.
[8] P. Aguiar, C.S. Adjimana, N.P. Brandon, J. Power Sources 138 (2004) 120–136.
[9] P. Lunghi, R. Bove, Fuel Cells: Fundam. Syst. 2 (2002) 83–91.
[10] S. Campanari, J. Power Sources 92 (2001) 26–34.
[11] P. Costamagna, K. Honegger, J. Electrochem. Soc. 145 (1998) 3995–4007.
[12] R. Bove, S. Ubertini, J. Power Sources 159 (2006) 543–559.
[13] E. Liese, R. Gemmen, F. Jabbari, J. Brouwer, Technical development issues and dynamic modeling of gas-turbine and fuel cell hybrid systems, ASME GT-360, 1999.
[14] E.A. Liese, R.S. Gemmen, T.P. Smith, C.L. Haynes, ASME Turbo Expo 2006: Power for Land Sea and Air, May 8–11, Barcelona, Spain, 2006.
[15] T.P. Smith, C.L. Haynes, W.J. Wepfer, D. Tucker, E.A. Liese, ASME International Mechanical Engineering Congress and Exposition, November 5–10, Chicago, IL, USA, 2006.
[16] R. Roberts, J. Brouwer, ASME J. Fuel Cell Sci. Technol. 3 (2006) 18–25.
[17] R. Roberts, J. Brouwer, T. Junker, H. Ghezel-Ayagh, J. Power Sources 161 (2006) 484–491.
[18] T. Kaneko, J. Brouwer, G. Samuelsen, J. Power sources 160 (2006) 316–325.
[19] F. Mueller, J. Brouwer, F. Jabbari, G. Samuelsen, ASME J. Fuel Cell Sci. Technol. 3 (2006) 144–154.
[20] J. Freeh, J. Pratt, J. Brouwer, Development of a solid oxide fuel cell/gas turbine hybrid system model for aerospace applications, ASME GT2004-53616, 2004.
[21] N. Dekker, B. Rietveld, J. Laatsch, F. Tietz, Proceedings of the 6th European Solid Oxide Fuel Cell Forum, Lucerne, Switzerland, 2004.
[22] M. Bahrami, M.M. Yovanovich, J.R. Culham, Proceedings of the 3rd International Conference on Microchannels and Minichannels, June 13–15, Toronto, Ontario, 2005.
[23] K. Wark, K. Wark Jr., Advanced Thermodynamics for Engineers, McGraw Hill, New York, 1994.